

# Radiatively limited dephasing and exciton dynamics in MoSe<sub>2</sub> monolayers

Tomasz Jakubczyk,<sup>†,‡</sup> Valentin Delmonte,<sup>†,‡</sup> Maciej Koperski,<sup>¶,§</sup> Karol  
Nogajewski,<sup>¶</sup> Clément Faugeras,<sup>¶</sup> Wolfgang Langbein,<sup>||</sup> Marek Potemski,<sup>¶</sup> and  
Jacek Kasprzak<sup>\*,†,‡</sup>

*Université Grenoble Alpes, Institut Néel, F-38000 Grenoble, France, CNRS, Institut Néel,  
"Nanophysique et semiconducteurs" group, F-38000 Grenoble, France, Laboratoire National des  
Champs Magnétiques Intenses, CNRS-UGA-UPS-INS-EMFL, 25 Av. des Martyrs, 38042  
Grenoble, France, Institute of Experimental Physics, Faculty of Physics, University of Warsaw, ul.  
Pasteura 5, 02-093 Warsaw, Poland, and Cardiff University School of Physics and Astronomy,  
The Parade, Cardiff CF24 3AA, UK*

E-mail: jacek.kasprzak@neel.cnrs.fr

## Abstract

By implementing four-wave mixing (FWM) micro-spectroscopy we measure coherence and population dynamics of the exciton transitions in monolayers of MoSe<sub>2</sub>. We reveal their dephasing times  $T_2$  and radiative lifetime  $T_1$  in a sub-picosecond (ps) range, approaching

---

\*To whom correspondence should be addressed

<sup>†</sup>Université Grenoble Alpes, Institut Néel, F-38000 Grenoble, France

<sup>‡</sup>CNRS, Institut Néel, "Nanophysique et semiconducteurs" group, F-38000 Grenoble, France

<sup>¶</sup>Laboratoire National des Champs Magnétiques Intenses, CNRS-UGA-UPS-INS-EMFL, 25 Av. des Martyrs, 38042 Grenoble, France

<sup>§</sup>Institute of Experimental Physics, Faculty of Physics, University of Warsaw, ul. Pasteura 5, 02-093 Warsaw, Poland

<sup>||</sup>Cardiff University School of Physics and Astronomy, The Parade, Cardiff CF24 3AA, UK

$T_2=2T_1$ , and thus indicating radiatively limited dephasing at a temperature of 6 K. We elucidate the dephasing mechanisms by varying the temperature and by probing various locations on the flake exhibiting a different local disorder. At a nanosecond range, we observe the residual FWM produced by the incoherent excitons, which initially disperse towards the dark states, but then relax back to the optically active states within the light cone. By introducing polarization-resolved excitation, we infer inter-valley exciton dynamics, showing an initial polarization degree of around 30%, constant during the initial sub-picosecond decay, followed by the depolarization on a picosecond timescale. The FWM hyperspectral imaging reveals the doped and undoped areas of the sample, allowing to investigate the neutral exciton, the charged one or both transitions at the same time. In the latter, we observe the exciton-trion beating in the coherence evolution indicating their coherent coupling.

**Keywords:** excitons, coherent nonlinear spectroscopy, transition-metal dichalcogenides,  $\text{MoSe}_2$ , four-wave mixing, coherent nonlinear spectroscopy

**Introduction** The identification of atomically-thin solids<sup>1</sup> resulted in the development of the intriguing physics of graphene, followed by the emerging technological applications.<sup>2,3</sup> Also, it stimulated a rapid progress in fundamental studies of thin films extracted from other than graphite layered materials, such as, semiconducting transition metal dichalcogenides (S-TMDs). The bandgap of S-TMDs, converts from indirect to direct, when reducing the material thickness to a single monolayer,<sup>4</sup> enabling exceptionally strong excitonic transitions. Owing to the breakdown of out of plane translational symmetry for two dimensional systems, the coupling of excitons with light is boosted,<sup>5</sup> resulting in their short radiative lifetime and thus increased oscillator strength  $\mu$ . Excitons in S-TMD monolayers display large binding energies  $E_B$  of several hundreds of meV<sup>6-9</sup> - an increase by one to two orders of magnitude with respect to a typical semiconductor quantum well.<sup>10,11</sup> The observed excitonic absorption in S-TMDs reaches the values as high as 10%,<sup>12</sup> illustrating an exceptionally strong  $\mu$  in these systems and implying a radiative lifetime in the sub-picosecond (sub-ps) range,<sup>13</sup> as recently observed in monolayers of  $\text{WSe}_2$ <sup>14,15</sup> and other emerging

two-dimensional systems, namely nano-platelets.<sup>27</sup> The robust coupling with light is attractive in prospective applications, especially for photodetectors.<sup>3</sup> It is also appealing in optical fundamental studies, for instance in polaritonics<sup>16</sup> and nonlinear spectroscopy.<sup>15,17,19</sup>

The large  $\mu$  in S-TMDs gives rise to a giant nonlinear optical response, which is investigated in this work via three-pulse four-wave mixing (FWM) micro-spectroscopy. This approach offers a direct access to the exciton coherence and population dynamics with a time resolution limited only by the duration of the laser pulses, which resonantly excite targeted optical transitions. Indeed, time-resolved non-resonant photoluminescence measurements,<sup>18</sup> offer insufficient time-resolution to infer sub-ps evolution and involve complex relaxation pathways. Instead, resonant experiments,<sup>15,19</sup> also investigating internal transitions<sup>14</sup> occurring in the THz domain, have recently revealed ultrafast radiative recombination of the exciton ground state in WSe<sub>2</sub>.

In this work, we show that the optical dephasing time  $T_2$  of the neutral exciton transition (EX) in a monolayer of MoSe<sub>2</sub> is intrinsically limited by the EX ultrafast radiative recombination  $T_1$ . In contrast to previous works inferring optical coherence in S-TMDs,<sup>15,19</sup> we take advantage of the micro-spectroscopy approach, employing the laser beams focused down to the diffraction limited size of  $0.7\ \mu\text{m}$  (full width at half-maximum, FWHM). Such implementation is used to perform the FWM hyperspectral imaging,<sup>20</sup> which discriminates the exciton charge state across the sample and helps to reveal the striking features of coherent coupling between the neutral and charged excitons. We demonstrate that the EX linear response inferred via micro-reflectance, is affected by the inhomogeneous broadening  $\xi$  also on a sub- $\mu\text{m}$  scale, evidenced by the photon echo formation in the FWM transients.<sup>21</sup> The analysis of the FWM delay dependence yields  $T_2 \simeq 2T_1$ , occurring on a sub-picosecond timescale. A spatially-resolved study shows that  $T_2$  depends on the local disorder, generating spatially varying localization potentials for excitons and thus varying  $\xi$ , directly influencing  $T_1$ . From the temperature dependent homogenous linewidth, retrieved from the measured coherence dynamics, we determine the dephasing due to phonon interaction, which is described by a linear part and a thermally activated part, as is quantum wells. We also monitor the density dynamics of excitons, which is governed by the interplay between bright states within

the light cone and various available dark states.

**Sample & experiment** An image of the studied MoSe<sub>2</sub> monolayer is shown in Fig. 2. It was exfoliated from bulk material and transferred onto a Si/SiO<sub>2</sub> substrate, with a nominal SiO<sub>2</sub> thickness of 86 nm. Relatively large monolayer flakes of up to  $(50 \times 50) \mu\text{m}^2$  size have been fabricated and placed in an optical He-flow cryostat. To infer both the coherence and the population dynamics of excitons, we retrieved their FWM by implementing a three-beam configuration<sup>20</sup> of the heterodyne spectral interferometry.<sup>21</sup> This technique has been proven as an efficient detection scheme of optical nonlinearities in a solid, until now only employed to retrieve wave mixing signals generated by individual transitions in semiconductor quantum dots.<sup>20,21,25</sup> FWM is an optical polarization created with short, resonant driving pulses;  $\mathcal{E}_1$ ,  $\mathcal{E}_2$  and  $\mathcal{E}_3$ , as depicted in Fig. 1 a. In the third-order ( $\chi^{(3)}$ ) regime its amplitude is proportional to  $\mu^4 \mathcal{E}_1^* \mathcal{E}_2 \mathcal{E}_3$ . Thus, owing to a large  $\mu$ , a dramatic enhancement of FWM is expected in MoSe<sub>2</sub> monolayers. Note that the \* stands for the complex conjugate, which is the origin of the FWM rephasing in inhomogeneously broadened systems,<sup>21</sup> generating the photon echo (as also sketched in Fig. 1 a), which acts as a probe of the microscopic dephasing. Micro-FWM spectroscopy requires the co-linear arrangement of the driving fields  $\mathcal{E}_{1,2,3}$ , which is enabled by phase-selecting the signal through optical heterodyning.<sup>21</sup> By employing acousto-optic modulation,  $\mathcal{E}_{1,2,3}$  are frequency up-shifted by radio-frequencies, introducing controlled phase-drifts in their respective pulse trains generated by a Ti:Sapphire femto-second laser. As we intend to measure sub-ps dynamics, pulseshaping<sup>20</sup> has been applied to correct the temporal chirp. After acquiring the delays  $\tau_{12}$  and  $\tau_{23}$ , introduced by a pair of mechanical delay lines,  $\mathcal{E}_{1,2,3}$  are recombined into a common spatial mode and are focused on the sample with the microscope objective. The reference beam  $\mathcal{E}_r$ , used in the heterodyne mixing and interferometric detection, is also focused at the sample, yet is displaced with respect to  $\mathcal{E}_{1,2,3}$ , as depicted in Fig. 2 a. The time-ordering of the pulses is presented on Fig. 1 a: measuring time-integrated FWM detected at the  $\Omega_3 + \Omega_2 - \Omega_1$  heterodyne frequency, as a function of  $\tau_{12}$  ( $\tau_{23}$ ), yields the coherence (population) dynamics of an optical transition. The FWM signal

is measured in reflectance, attaining a shot-noise detection limit and rejecting the resonant driving fields  $\mathcal{E}_{1,2,3}$  with  $10^6$  ( $10^{12}$ ) selectivity in field (intensity). The interference between the heterodyned signal and  $\mathcal{E}_r$  is spectrally resolved with an imaging spectrometer. Further details regarding the current experimental implementation are given in Ref. [20].

In Fig. 1 b we present a typical spectral interference between  $\mathcal{E}_r$  and the FWM at a temperature  $T=5$  K for  $\tau_{12} = 0$ . The FWM intensity is retrieved by spectral interferometry and shown in Fig. 1 c. The signal consists of two transitions identified as the ground state - exciton (EX) and the single electron - trion transitions (TR).<sup>22</sup> In Fig. 1 d we present the FWM intensity of EX as a function of  $\mathcal{E}_1$  intensity demonstrating a linear dependence in the  $\chi^{(3)}$  regime, as expected. Note that the FWM can be driven with a  $\mathcal{E}_1$  intensity as low as a few tens of nW, corresponding to a few hundreds of photons per pulse  $\mathcal{E}_1$  and generating a low carrier density, less than  $10^9/\text{cm}^2$ . Such density is far below the saturation density<sup>23</sup> estimated at around  $10^{13}/\text{cm}^2$ . In our study, we therefore consider the creation of excitons with  $K \sim 0$  center of mass momentum, which appear at the, K+ and K-, points of the Brillouin zone of the S-TMD crystal. Those excitons can either decay radiatively or disperse out of the light cone ( $K > n\omega/c$ ) via phonon scattering. The latter process occupies dark exciton states, which relax back to  $K < n\omega/c$  on a pico-second time scale and eventually recombine. Further relaxation pathways are scattering electrons and holes between the K-points.

**Hyperspectral imaging** The micro-spectroscopy approach enables to perform FWM hyperspectral imaging,<sup>20,25</sup> as shown in Fig. 2. It allows to identify regions of the flake dominated by the FWM of EX or TR (see Fig. 2 b and c). Clearly, the two images are complementary, which permits to distinguish regions of different resident carrier concentration. In Fig. 2 b we note that the FWM amplitude remains virtually constant over the areas of more than  $(5 \times 5) \mu\text{m}^2$ , indicating weak disorder and thus enabling an extremely fast radiative decay of excitons. In the following experiments, the performed imaging allowed us to selectively address EX or TR, or to drive simultaneously both transitions. Performing micro-spectroscopy also permits to locally address sub- $\mu\text{m}$  regions of smaller spectral inhomogeneous broadening with respect to the total area of the flake.

To exemplify this, we have performed a statistical analysis of the micro-photoluminescence (PL) hyperspectral imaging. Similarly as in Fig. 1 c, confocally detected PL spectra yield EX and TR transitions, as displayed at the top of Fig. 2 d. We observe particularly bright emission, with spectrally integrated count rate of typically 350 kHz from each transition. For every spatial position, we have determined the integrated intensity for both transitions and their center energies. For the latter, we observe the spread over  $\xi \simeq 10 \text{ meV}$ , as displayed at the bottom of Fig. 2 d. Interestingly, despite this large, macroscopic  $\xi$  - which we attribute to the strain distribution across the flake - the trion binding energy  $\Delta$  remains well defined,  $\Delta = (28.8 \pm 0.3) \text{ meV}$ . We note that the lower the TR transition energy, the higher its intensity is measured, which is attributed to the the distribution of residual electrons in the sample. Interestingly, such correlation is not observed for EX, i.e., the EX intensity is not sensitive to the apparent, in our sample changes in the charge density. In Fig. 2 e and f we present the PL imaging spectrally integrated over EX and TR transition, respectively. By comparing it with Fig. 2 b and c, we point out two advantages of the FWM imaging with respect to the PL one. Firstly, owing to the third-power scaling of the FWM intensity with the excitation power, combined with heterodyning with  $\mathcal{E}_r$ , the spatial resolution in the FWM imaging is enhanced<sup>26</sup> up to  $0.3\lambda/\text{NA} \approx 360 \text{ nm}$ , surmounting the standard diffraction limit by a factor of 2. Secondly, the FWM yields a significantly improved imaging selectivity of EX and TR across the flake. In fact, different properties are inferred in both experiments. The FWM directly probes  $\mu$  of the resonantly generated excitons at the K-points of the valleys. Instead, the non-resonant PL reflects more complex carrier relaxation along the valleys towards their K-points, prior to the exciton formation, followed by their radiative recombination.

**Coherence dynamics** The strength of the FWM spectroscopy in assessing the coherence in solids lies in its capability to separate homogenous ( $\gamma$ ) and inhomogeneous ( $\xi$ ) contributions of the transition's spectral width. In particular, in a presence of  $\xi$ , the time-resolved FWM amplitude exhibits a photon echo,<sup>15,27</sup> which decays as  $\exp(-2\tau_{12}/T_2)$ . Hence, to investigate the exciton coherence dynamics, we measured degenerate FWM ( $\Omega_2 = \Omega_3$ ), as a function of  $\tau_{12}$ . Time-resolved

FWM amplitude of the EX transition, displayed in Fig. 3 a, clearly demonstrates formation of the photon echo. From its temporal width we estimate the local  $\xi$  to be in the meV range (around 3 meV for the case shown in Fig. 3 a). Fig. 3 b shows the time-integrated FWM as a function of  $\tau_{12}$ . The data are modeled by a convolution of a Gaussian profile with an exponential decay. The former exhibits the FWHM width of 0.16 ps, reflecting duration of  $\mathcal{E}_{1,2,3}$  impinging the sample. Instead, from the latter we retrieve at T=6 K the dephasing time  $T_2 = 2\hbar/\gamma = (620 \pm 20)$  fs, and thus  $\gamma \simeq 2.1$  meV (FWHM). For simplicity, the dynamics owing to the echo formation process close to zero delay, has been here disregarded, yet it explains a minor deviation between the measurement and prediction. The homogenous broadening  $\gamma$  is around twice smaller than the transition linewidth directly measured via micro-reflectivity, as shown in the inset of Fig. 3 b and also in FWM (see Fig. 1 c). We thus conclude that the line-shape remains affected by the inhomogeneous broadening  $\xi$ , even though a sub- $\mu\text{m}$  area is probed. With increasing temperature,  $T_2$  is expected to decrease,<sup>15</sup> owing to phonon scattering. This is highlighted in Fig. 3 b. At T=45 K the dephasing accelerates and we measure  $T_2 = (520 \pm 40)$  fs. At ambient temperature the dephasing occurs at a timescale faster than 100 fs and is not resolved by our setup, although a pronounced FWM is still measured. We note that for the TR transition at T=6 K we find  $T_2 = (460 \pm 30)$  fs and similar inhomogeneous broadening as for EX, also generating a photon echo as in Fig. 3 c (not shown). This shorter dephasing of the charged exciton, is tentatively interpreted in terms of the final state damping, due to the energy distribution of final state energies of the leftover electron. In Fig. 3 c we present the coherence dynamics measured at the boundary of the doped and undoped regions of the flake, marked with a cross in Fig. 2 d, such that the FWM of both EX and TR is driven in tandem. We observe a beating, withstanding on both transitions during initial positive delays  $\tau_{12}$ , up to around 700 fs when the TR coherence virtually vanishes. The beating period of  $\zeta = 140$  fs (marked with a pair of vertical lines), well corresponds to the EX - TR binding energy  $\Delta = 2\pi\hbar/\zeta \simeq 29$  meV and thus indicates their coherent coupling.<sup>28</sup> To support this statement - and in particular, to distinguish between polarization interference and coherent coupling<sup>25</sup> - the data have been Fourier-transformed along the delay  $\tau_{12}$  to yield the two-dimensional FWM spectrum,

indeed revealing off-diagonal coupling terms between EX and TR (not shown).

To gain a deeper understanding of the exciton ultrafast dynamics, we have combined the enhanced spatial and temporal resolution of our experiment and we have performed spatially-resolved dephasing study at  $T=6$  K. Within an area of  $8\text{ }\mu\text{m}$  by  $8\text{ }\mu\text{m}$ , displaying uniquely the EX transition, we have scanned the coherence dynamics with a spatial step of  $0.66\text{ }\mu\text{m}$ . The analysis of the obtained statistics of dephasing (169 traces), reveals variations of  $T_2$  within the probed area from around  $0.5\text{ ps}$  up to  $1.5\text{ ps}$ . Interestingly, the locations on the flake yielding the shortest  $T_2$  also display the broadest photon echo, and thus the smallest  $\xi$ . Conversely, the longest  $T_2$  is measured on the areas characterized by a larger  $\xi$ , and thus showing the narrowest photon echo, here limited by the temporal duration of the laser pulses. An example of such two representative cases is displayed in Fig. 4 a and b. The spatially-resolved dephasing experiment indicates that  $T_2$  is governed by a local disorder, realizing various localization potentials. The resulting spatially-dependent coherence volume of EX has a direct impact on its radiative lifetime  $T_1$ : the fastest recombination is expected at the areas of the smallest  $\xi$ , as indeed measured. Full spatial correlations between  $T_1$ ,  $T_2$  and  $\xi$  will be reported in a forthcoming publication. In Fig. 4 c we present the coherence dynamics on the chosen area exhibiting an increased  $T_2$ , measured from  $6\text{ K}$  to  $150\text{ K}$ . The data clearly show a gradual decrease of  $T_2$  with temperature from  $1.4\text{ ps}$  to  $0.2\text{ ps}$  respectively. The retrieved  $\gamma = 2\hbar/T_2$  is plotted in the inset. It can be modeled with a linear dependence and an additional bosonic term:<sup>41</sup>  $\gamma(T) = \gamma_0 + aT + b/(\exp(E_1/k_B T) - 1)$ . The linear term ( $\gamma_0 = (0.78 \pm 0.11)\text{ meV}$ ,  $a = (0.03 \pm 0.003)\text{ meV/K}$ ) is due to low energy acoustic phonons. The latter term, with the energy ( $E_1 = 43 \pm 4\text{ meV}$  and  $b = (187 \pm 75)\text{ meV}$ , could be attributed to thermal activation of higher energy optical phonons.<sup>41</sup>

**Population dynamics** In the following, the FWM is employed to infer the EX population dynamics after their resonant and selective excitation in a given valley ( $\mathcal{E}_1$  and  $\mathcal{E}_2$ , denoted as  $\mathcal{E}_{1,2}$ , are co-circularly polarized). They arrive at the flake with virtually no delay,  $\tau_{12} = (50 \pm 10)\text{ fs}$ , generating exciton population. Owing to the large  $\mu$ , the excitons exhibit fast radiative decay, yet



also are subject to scattering on lattice defects and phonons. The matrix element for the Coulomb induced, parametric exciton-exciton scattering is proportional to the square of an exciton Bohr radius.<sup>29</sup> We thus propose that the Coulomb scattering is reduced for these spatially compact excitons. In particular, this channel is negligible for the small exciton densities employed here. Nevertheless, excitons still experience scattering<sup>24</sup> for instance induced by defects, disorder and phonons, which can efficiently redistribute them out of the light cone (marked with dashed lines in the inset of Fig. 3 c), toward  $K > n\omega/c$ . This type of scattering is particularly efficient in S-TMDs: due to heavy masses (and thus flat bands at the bottom of the branches) and large  $\gamma$ , the excitons' center of mass scatter out of the light cone at practically no cost in energy. As a result, one part of the created population instantly decays with its radiative lifetime  $T_1$ , while the remaining part spreads along the dispersion branch populating dark states (i.e. outside the light cone) or is scattered into one of the counter-polarized valleys involving spin-flip processes. Also a part of these excited excitons eventually relax toward the bottom of the valley with a characteristic time  $T_{\text{intra}}$  and recombine radiatively, as depicted in Fig. 3 c. In the dynamics probed with FWM, we disregard the influence of strongly localized, quantum-dot like states, due to their small density (not detected on the region shown in Fig. 2). For simplicity, we also disregard non-radiative Auger processes,<sup>14</sup> as we operate at low exciton densities.

The FWM, triggered by  $\mathcal{E}_3$  from the density grating generated by  $\mathcal{E}_1$  and  $\mathcal{E}_2$ , therefore probes all the above mentioned processes via  $\tau_{23}$  dependence. This is shown in Fig. 3 c, for the EX (obtained the same spatial position as in Fig. 3 b) for driving upon co-circular polarization of  $\mathcal{E}_{1,2,3}$ . The data are modeled with a double exponential decay convoluted with the Gaussian laser pulse, showing temporal width of 0.16 ps (FWHM). From the initial decay we retrieve the exciton lifetime of  $T_1 = (390 \pm 20)$  fs, while the FWM for further delays  $\tau_{23}$  yields the intra-valley relaxation time of  $T_{\text{intra}} = (4.3 \pm 0.6)$  ps. At  $T=45$  K we measure instead  $(T_1, T_{\text{intra}})=(0.42 \pm 0.01, 6.84 \pm 0.38)$  ps. An increase of  $T_{\text{intra}}$  with temperature is attributed to Boltzmann distribution of excitons, allowing for reaching higher energies and K-vectors out of the light cone, and also to access different dark states offered by the complex structure of the valley-excitons. A physical picture arising from the

FWM experiment at low temperature is that the initial exciton decay with the time  $T_1$ , covering an order of magnitude in amplitude (see Fig. 3 c), is due to the radiative recombination, while the non-radiative processes are of minor impact. Importantly, comparing the  $T_1$  with  $T_2$  times, we conclude that the dephasing is principally due to the radiative decay, nearing to the radiative limit - the data can also be well modeled by fixing  $T_2=2T_1$  and using  $T_{\text{intra}}$  as the only fitting parameter. Observation of the radiatively limited dephasing is a prerequisite for implementing more advanced optical coherent control schemes in S-TMDs.

We point out that the dynamics of the secondary, incoherent excitons - here probed by  $\tau_{23}$  dependence of FWM - is particularly complex and might be influenced by a set of unconventional features present in S-TMDs. One should bear in mind coupling with and scattering toward counter-polarized K-valleys and spin-split bands, relevant in formation of exciton complexes. In fact, triple-degeneracy of the K-valleys, enables various configurations for bright and dark excitons states, as previously considered for other systems hosting multi-excitons.<sup>30,31</sup> We also point out exotic dispersion relations for the center-of-mass momentum.<sup>32</sup> Thus, we refrain from firm interpretation and first-principle modeling of the secondary exciton dynamics, displayed in Fig. 5 on a 100 ps time scale.

**Inter-valley dynamics** Below, we present the FWM results obtained upon polarization-resolved driving, employed to investigate exciton scattering between counter-polarized valleys, testing the robustness of the pseudo-spin degree of freedom. The reciprocal space of TMDs monolayers displays nonequivalent bands with the extrema at  $K$ -points,<sup>33-35</sup> labeled as  $K_+$  and  $K_-$ . The dipole-allowed transitions in these two valleys can be selectively addressed by circularly polarized light,  $\sigma^+$  and  $\sigma^-$ , respectively. The light helicity is therefore considered as an asset to drive, manipulate and read the state of the valley subspaces. The valley polarization,<sup>34</sup> although protected by the strong spin-orbit splitting in the valence band, decays mainly due to the to electron-hole exchange interaction.<sup>36,37</sup> Since the stability of this degree of freedom is required in prospective applications of TMDs, intense efforts are currently devoted to study its dynamics and to reveal the mechanisms

that govern it,<sup>38</sup> in particular in a presence of spin-forbidden transitions.<sup>12,39,42–44</sup>

To infer the exciton inter-valley dynamics, we implemented polarization-resolved excitation of the FWM signal. The polarization state of the beams is adjusted by a set of  $\lambda/2$  and  $\lambda/4$  plates, by monitoring spectral interferences of  $\mathcal{E}_{1,2,3}$  with  $\mathcal{E}_r$ . Specifically,  $\mathcal{E}_3$  and  $\mathcal{E}_r$  are set as co-circular and thus yield a maximal contrast of the heterodyne spectral fringes. Instead, the polarization state of  $\mathcal{E}_{1,2}$  is rotated until the interference contrast is minimized, yielding opposite circular polarizations for  $\mathcal{E}_{1,2}$  (creating exciton population in the  $K_+$ ) and  $\mathcal{E}_3$  (converting the population, redistributed from  $K_+$  into  $K_-$ , toward the FWM). To probe the exciton dynamics in the same valley (as in Fig. 3 c of the manuscript), we set the co-circular polarization of  $\mathcal{E}_{1,2}$  and  $\mathcal{E}_3$ , by maximizing the spectral interference of  $\mathcal{E}_{1,2}$  and  $\mathcal{E}_r$ . We estimate the polarization cross-talk between  $\mathcal{E}_{1,2}$  and  $\mathcal{E}_3$  around  $6 \times 10^{-4}$ . Thus, polarization selective driving permits to probe the dynamics of the exciton transfer towards a counter-polarized valley, as depicted in Fig. 5, and thus to test the robustness of the valley pseudo-spin.<sup>35</sup>

The measurement is presented in Fig. 5 (bottom). As in Fig. 3 c, we observe an initial fast decay of the radiatively recombining excitons within the first ps and subsequent recombination of the secondary excitons. The early dynamics for both polarization configuration is not the same during initial several ps of  $\tau_{23}$ . Instead, for longer delays,  $\tau_{23} > 10$  ps, the measured FWM (generated by the secondary excitons) is the same for both driving configurations. We calculate the FWM circular polarization degree, which we define as  $\rho(\tau_{23}) = \frac{R(\tau_{23}, \sigma+) - R(\tau_{23}, \sigma-)}{R(\tau_{23}, \sigma+) + R(\tau_{23}, \sigma-)} \times 100\%$ , where  $R$  denotes the spectral FWM amplitude. The resulting  $\rho(\tau_{23})$  is plotted at the top of Fig. 5. We thus do observe a significant pseudo-spin polarisation around zero delay,  $\rho(\tau_{23} \simeq 0) \simeq 30\%$ , which however vanishes extremely rapidly, within around 5 ps, such that  $\rho(\tau_{23}) = 0$  for  $\tau_{23} > 10$  ps. This result brings a new input (demonstration of a possibility to create valley-polarized excitons, but their rapid depolarization) towards a firm understanding of an intriguingly weak efficiency of optical pumping in MoSe<sub>2</sub> monolayers (in contrast to other S-TMDs).<sup>45</sup> The polarization degree, relevant for valleytronics applications, could be stabilized by using magnetic fields<sup>38</sup> or by fabricating more involved hetero-structures<sup>46,47</sup> based on S-TMDs. When analyzing Fig. 5 it is worth to note

a large fraction of the FWM response within initial several ps for both polarization configurations, as compared to the subsequent dynamics. This shows that the exciton density is mainly removed radiatively within the sub-ps radiative lifetime  $T_1$ , as discussed before.

**Conclusions** By performing FWM spectroscopy, we have demonstrated a giant, optical, coherent, nonlinear response of exciton transitions in MoSe<sub>2</sub> monolayers. We find an increase in the FWM amplitude by two orders of magnitude, as compared to a high quality CdTe semiconductor quantum well (not shown), emitting at the similar wavelength and driven with a comparable excitation power. Taking advantage of the microscopy approach, we have performed the hyper-spectral imaging, which allowed us to accurately determine the areas yielding FWM responses of either neutral, or charged excitons, or both. Electrical gating of such structures could enable spectral control of coherent responses from TMDs, providing insights into the mutual influence of TR and EX onto their dynamics. Using two-beam FWM micro-spectroscopy, we have measured the excitons' coherence evolution, accessing dephasing times  $T_2$ , which turn out to be intrinsically limited by the radiative lifetime. The inhomogeneous broadening  $\xi$  on a sub- $\mu\text{m}$  range is reduced by an order of magnitude with respect to  $\xi$  measured on the entire size of the flake, although still gives rise to the pronounced photon echo. We have also shown that  $T_2$  spatially varies across the flake, as the  $T_1$  is governed by the local disorder, determining the exciton localization. Prospective experiments, exploiting two-dimensional FWM spectroscopy, will ascertain coupling mechanisms between exotic valley-exciton species (excitons, trions, biexcitons and multiexcitons) offered by S-TMDs. Our approach could be used to retrieve coherent responses of the localized exciton states in S-TMDs,<sup>48</sup> which are expected to exhibit ultra-long dephasing.<sup>49</sup> Finally, by exploiting polarization-resolved, three-beam FWM we assessed the exciton population dynamics, revealing the interplay between the sub-ps radiative decay  $T_1$  and the intra-valley relaxation  $T_{\text{intra}}$  of the excitons scattered towards the dark states, revisiting the light-matter coupling in two-dimensional systems.<sup>5</sup>

*We acknowledge the support by the ERC Starting Grant PICSSEN contract no. 306387 and the*

ERC Advanced Grant MOMB contract no. 320590. We thank G. Nogues and M. Richard for helpful remarks on the manuscript. We also acknowledge the support from Nanofab facility of the Institute Néel, CNRS UGA. Monolayers of  $\text{MoSe}_2$  were obtained by means of polydimethylsiloxane-based exfoliation of bulk crystals purchased from HQ Graphene.

## References

- (1) Novoselov, K. S.; Geim, A. K.; Morozov, S. V.; Jiang, D.; Zhang, Y.; Dubonos, S. V.; Grigorieva, I. V.; Firsov, A. A. *Science* **2004**, *306*, 666–669.
- (2) Fiori, G.; Bonaccorso, F.; Iannaccone, G.; T.Palacios,; Neumaier, D.; Seabaugh, A.; Banerjee, S. K.; Colombo, L. *Nat. Nanotech.* **2014**, *10*, 768–779.
- (3) Koppens, F. H. L.; Mueller, T.; Avouris, P.; Ferrari, A. C.; Vitiello, M. S.; Polini, M. *Nat. Nanotech.* **2014**, *10*, 780–793.
- (4) Mak, K. F.; Lee, C.; Hone, J.; Shan, J.; Heinz, T. F. *Phys. Rev. Lett.* **2010**, *105*, 136805.
- (5) Deveaud, B.; Clérot, F.; Roy, N.; Satzke, K.; Sermage, B.; Katzer, D. S. *Phys. Rev. Lett.* **1991**, *67*, 2355.
- (6) Ye, Z.; Cao, T.; O’Brien, K.; Zhu, H.; Yin, X.; Wang, Y.; Louie, S.G.; Zhang, X.; *Nature* **2014**, *513*, 214–218.
- (7) Chernikov, A.; Berkelbach, T.C.; Hill, H.M.; Rigosi, A.; Li, Y.; Aslan, O.B.; Reichman, D.R.; Hybertsen, M.S.; Heinz, T.F. *Phys. Rev. Lett.* **2014**, *113*, 076802.
- (8) Wang, G.; Marie, X.; Gerber, I.; Amand, T.; Lagarde, D.; Bouet, L.; Vidal, M.; Balocchi, A.; Urbaszek, B. *Phys. Rev. Lett.* **2015**, *114*, 097403.
- (9) Olsen, T.; Latini, S.; Rasmussen, F.; Thygesen, K. S. *Phys. Rev. Lett.* **2016**, *116*, 056401.
- (10) Leavitt, R. P.; Little, J. W. *Phys. Rev. B* **1990**, *42*, 11774.

- (11) Andreani, L. C. In *Confined Electrons and Photons: New Physics and Applications*; Burstein, E., Weisbuch, C., Eds.; Nato Science Series: B Physics; Plenum Press: New York, 1995; Vol. 340; pp 57–112.
- (12) Arora, A.; Koperski, M.; Nogajewski, K.; Marcus, J.; Faugeras, C.; Potemski, M. *Nanoscale* **2015**, *7*, 10421–10429.
- (13) Palummo, M.; Bernardi, M.; Grossman, J. C. *Nano Lett.* **2015**, *15*, 2794.
- (14) Poellmann, C.; Steinleitner, P.; Leierseder, U.; Nagler, P.; Plechinger, G.; Porer, M.; Bratschitsch, R.; Schüller, C.; Korn, T.; Huber, R. *Nat. Mater.* **2015**, *14*, 889–893.
- (15) Moody, G.; Dass, C. K.; Hao, K.; Chen, C.-H.; Li, L.-J.; Singh, A.; Tran, K.; Clark, G.; Xu, X.; Berghäuser, G.; Malic, E.; Knorr, A.; Li, X. *Nat. Comm.* **2015**, *6*, 8315.
- (16) Liu, X.; Galfsky, T.; Sun, Z.; Xia, F.; chen Lin, E.; Lee, Y.-H.; Kéna-Cohen, S.; Menon, V. M. *Nat. Phot.* **2014**, *9*, 30–34.
- (17) Malard, L. M.; Alencar, T. V.; Barboza, A. P. M.; Mak, K. F.; de Paula, A. M. *Phs. Rev. B* **2013**, *87*, 201401(R).
- (18) Lagarde, D.; Bouet, L.; Marie, X.; Zhu, C. R.; Liu, B. L.; Amand, T.; Tan, P. H.; Urbaszek, B. *Phys. Rev. Lett.* **2014**, *112*, 047401.
- (19) Hao, K.; Moody, G.; Wu, F.; Dass, C. K.; Xu, L.; Chen, C.-H.; Li, M.-Y.; Li, L.-J.; MacDonald, A. H.; Li, X. *Nat. Phys.* doi:10.1038/nphys3674 **2016**,
- (20) Fras, F.; Mermillod, Q.; Nogues, G.; Hoarau, C.; Schneider, C.; Kamp, M.; Höfing, S.; Langbein, W.; Kasprzak, J. *Nat. Phot.* **2016**, *10*, 155.
- (21) Langbein, W.; Patton, B. *Phys. Rev. Lett.* **2005**, *95*, 017403.
- (22) Wang, G.; Palteau, E.; Amand, T.; Tongay, S.; Marie, X.; Urbaszek, B. *Appl. Phys. Lett.* **2015**, *106*, 112101.

- (23) Jones, A. M.; Yu, H.; Ghimire, N. J.; Wu, S.; Aivazian, G.; Ross, J. S.; Zhao, B.; Yan, J.; Mandrus, D. G.; Xiao, D.; Yao, W.; ; Xu, X. *Nat. Nanotech.* **2016**, 8, 634.
- (24) Langbein, W.; Runge, E.; Savona, V.; Zimmermann, R. *Phys. Rev. Lett.* **2002**, 89, 157401.
- (25) Kasprzak, J.; Patton, B.; Savona, V.; Langbein, W. *Nat. Phot.* **2011**, 5, 57-63.
- (26) Langbein, W. *Rivista del nuovo cimento* **2010**, 33, 255–312.
- (27) Naeem, A.; Masia, F.; Christodoulou, S.; Moreels, I.; Borri, P.; Langbein, W. *Phys. Rev. B* **2015**, 91, 121302(R).
- (28) Singh, A.; Moody, G.; Wu, S.; Wu, Y.; Ghimire, N. J.; Yan, J.; Mandrus, D. G.; Xu, X.; Li, X. *Phys. Rev. Lett.* **2014**, 112, 216804.
- (29) Porras, D.; Ciuti, C.; Baumberg, J. J.; Tejedor, C. *Phys. Rev. B* **2002**, 66, 085304.
- (30) Masia, F.; Langbein, W.; Moreels, I.; Hens, Z.; and Borri, P. *Phys. Rev. B* **2011**, 83, 201305(R).
- (31) An, J. M.; Franceschetti, A.; and Zunger, A. *Nano. Lett.* **2007**, 7, 2129.
- (32) Qiu, D. Y.; Cao, T.; Louie, S. G. *Phys. Rev. Lett.* **2015**, 115, 176801.
- (33) Xiao, D.; Liu, G.-B.; Feng, W.; Xu, X.; Yao, W. *Phys. Rev. Lett.* **2012**, 108, 196802.
- (34) Jones, A. M.; Yu, H.; Ghimire, N. J.; SanfengWu.; Aivazian, G.; Ross, J. S.; Zhao, B.; Yan, J.; Mandrus, D. G.; Xiao, D.; Yao, W.; Xu, X. *Nat. Nanotech.* **2013**, 8, 634–638.
- (35) Xu, X.; Yao, W.; Xiao, D.; Heinz, T. F. *Nat. Phys.* **2014**, 10, 343–350.
- (36) Yu, T.; Wu, M. W. *Phys. Rev. B* **2014**, 89, 205303.
- (37) Glazov, M. M.; Amand, T.; Marie, X.; Lagarde, D.; Bouet, L.; Urbaszek, B. *Phys. Rev. B* **2014**, 89, 201302(R).

- (38) Smoleński, T.; Goryca, M.; Koperski, M.; Faugeras, C.; Kazimierczuk, T.; Nogajewski, K.; Kossacki, P.; Potemski, M. *Phys. Rev. X* **2016**, 6, 021024
- (39) Zhang, X.-X.; You, Y.; Zhao, S. Y. F.; Heinz, T. F. *Phys. Rev. Lett.* **2015**, 115, 257403.
- (42) Wang, G.; Robert, C.; Suslu, A.; Chen, B.; Yang, S.; Alamdari, S.; Gerber, I. C.; Amand, T.; Marie, X.; Tongay, S.; Urbaszek, B. *Nat. Comm.* **2015**, 6, 10110.
- (41) Horzum, S.; Sahin, H.; Cahangirov, S.; Cudazzo, P.; Rubio, A.; Serin, T.; Peeters, F.M.; *Phys. Rev. B.* **2013**, 87, 125415.
- (42) Wang, G.; Robert, C.; Suslu, A.; Chen, B.; Yang, S.; Alamdari, S.; Gerber, I. C.; Amand, T.; Marie, X.; Tongay, S.; Urbaszek, B. *Nat. Comm.* **2015**, 6, 10110.
- (43) Echeverry, J. P.; Urbaszek, B.; Amand, T.; Marie, X.; Gerber, I. C. *arXiv:1601.07351* **2016**,
- (44) Withers, F. et al. *Nano Lett.* **2015**, 15, 8223–8228.
- (45) Dery, H.; and Song, Y. *Phys. Rev. B* **2015**, 92, 125431.
- (46) Rivera, P.; Schaibley, J. R.; Jones, A. M.; Ross, J. S.; Wu, S.; Aivazian, G.; Klement, P.; Seyler, K.; Clark, G.; Ghimire, N. J.; Yan, J.; Mandrus, D. G.; Yao, W.; Xu, X. *Nat. Comm.* **2015**, 6, 6242.
- (47) Rivera, P.; Seyler, K. L.; Yu, H.; Schaibley, J. R.; Yan, J.; Mandrus, D. G.; Yao, W.; Xu, X. *arXiv:1601.02641* **2016**,
- (48) Koperski, M.; Nogajewski, K.; Arora, A.; Cherkez, V.; Mallet, P.; Veuillen, J.-Y.; Marcus, J.; Kossacki, P.; Potemski, M. *Nat. Nanotech.* **2015**, 10, 503–506.
- (49) Schaibley, J. R.; Karin, T.; Yu, H.; Ross, J. S.; Rivera, P.; Jones, A. M.; Scott, M. E.; Yan, J.; Mandrus, D. G.; Yao, W.; Fu, K.-M.; Xu, X. *Phys. Rev. Lett.* **2015**, 114.



**Figures and captions:**

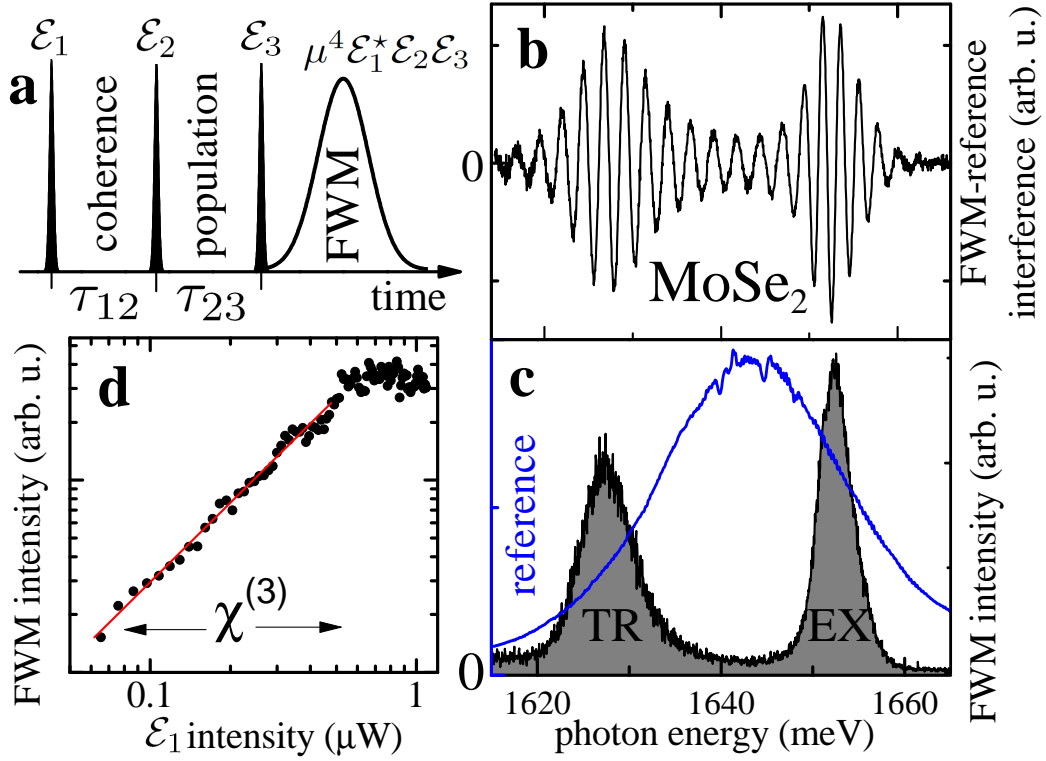


Figure 1: **Four-wave mixing spectroscopy of the MoSe<sub>2</sub> monolayer.** a) Pulse sequence employed in FWM experiments and related observables. b) FWM spectral interferogram obtained on the flake position displaying the exciton (EX) and trion (TR) transitions. c) FWM intensity (black) retrieved from b) via spectral interferometry.  $\mathcal{E}_r$  is shown with a blue line. d) Spectrally integrated FWM intensity of EX as a function of  $\mathcal{E}_1$  intensity, showing the driving range yielding the  $\chi^{(3)}$  regime of the FWM.

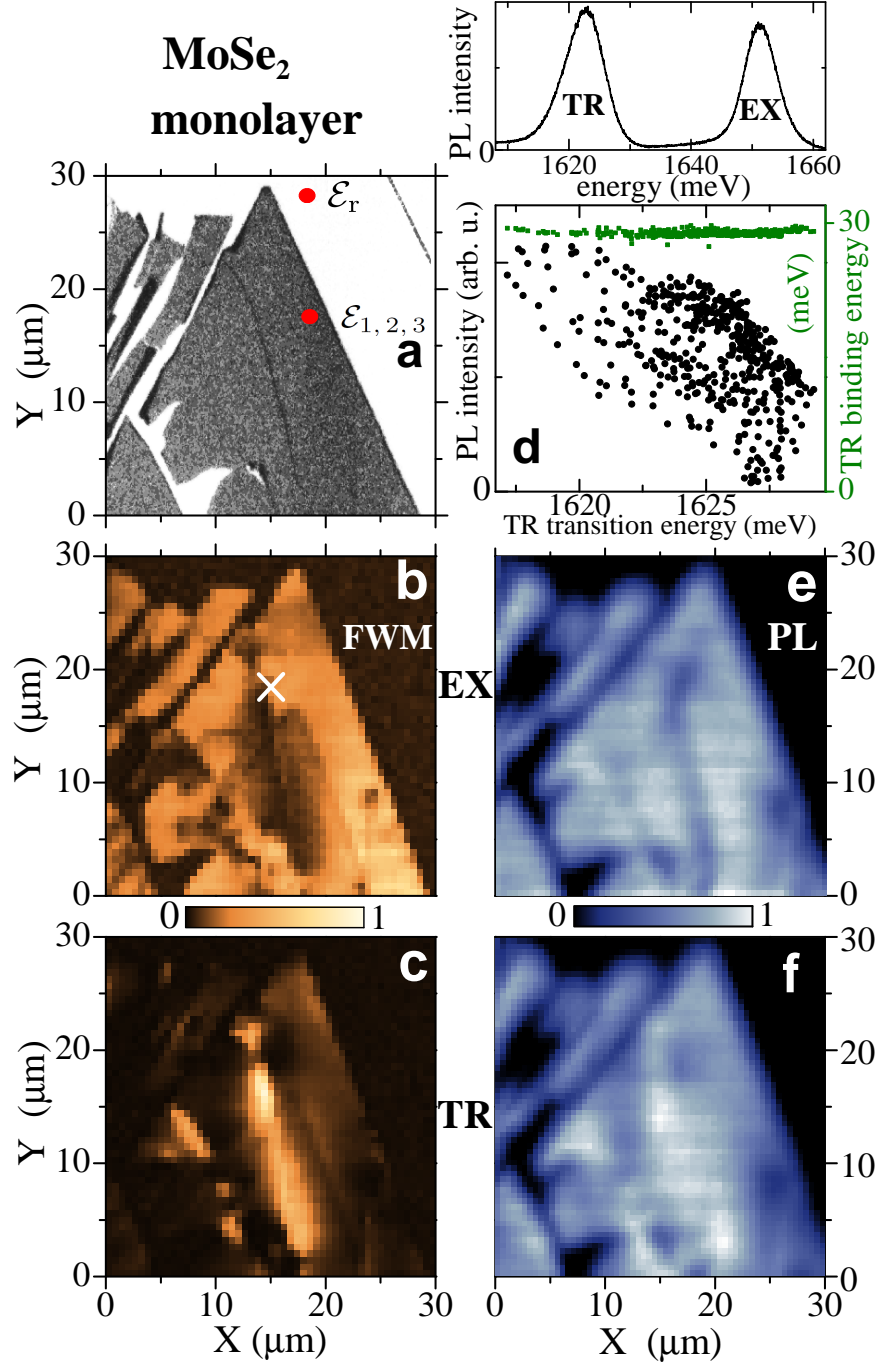


Figure 2: **Hyperspectral mapping of the MoSe<sub>2</sub> monolayer.** a) Optical contrast of the sample observed in reflectance. b)-c) Spatial imaging of the FWM amplitude, spectrally averaged over the exciton (b) response, centered at  $\sim 1650$  meV and the trion (c) at  $\sim 1625$  meV. Heterodyning at the FWM frequency  $\Omega_3 + \Omega_2 - \Omega_1$  with  $\tau_{12} = \tau_{23} = 50$  fs,  $T = 6$  K. d) Top: A typical PL spectrum, non-resonantly excited at  $\sim 1750$  meV ( $\sim 710$  nm) with  $\simeq 0.1$   $\mu$ W average power arriving at the sample surface, displaying bright emission from EX and TR, with integrated count rate of 350 kHz for each transition. Bottom: Correlation between the PL intensity of the TR (black) and its binding energy (green), as a function of its transition energy. e)-f) PL imaging of TR and EX, respectively. Excitation conditions as in d). Linear color scale, as shown by horizontal bars.

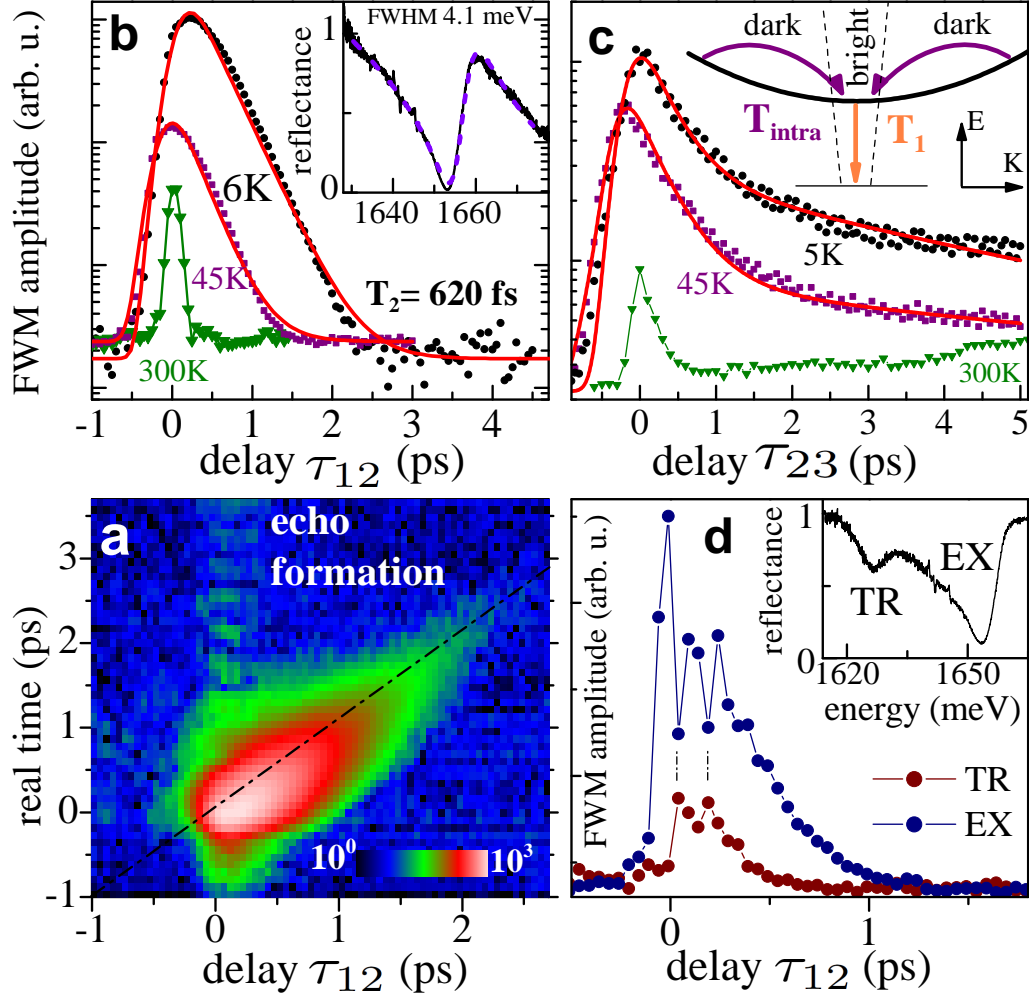


Figure 3: **Exciton dynamics in the MoSe<sub>2</sub> monolayer inferred with FWM microscopy.** a) Time-resolved FWM amplitude as a function of  $\tau_{12}$ , showing formation of a photon echo: a Gaussian signal with a maximum for  $t = \tau_{12}$ . Logarithmic color scale given by the color bar. b) FWM amplitude as a function of  $\tau_{12}$  retrieved from the EX at  $T = (6, 45, 300)$  K given by (black circles, purple squares and green triangles), respectively. The simulations yielding  $T_2 \simeq (620, 520)$  fs are given by red traces. Inset: reflectance measured at  $T = 6$  K yielding 4.1 meV FWHM. c) Cartoon of the considered radiative recombination and intra-valley relaxation processes is presented in the inset. The initial dynamics of the EX population measured at (5, 45, 300) K, color coding as in b). The results yield radiative lifetime  $T_1$  and relaxation time  $T_{\text{intra}}$  (see main text). d)  $\tau_{12}$  dependence of the FWM amplitude when simultaneously driving the EX (blue) and TR (brown) transitions, revealing a beating with 140 fs period, and thus indicating EX-TR coherent coupling. The location of the excitation is marked with a cross in Fig. 2 b, while the corresponding micro-reflectance spectrum is given in the inset.

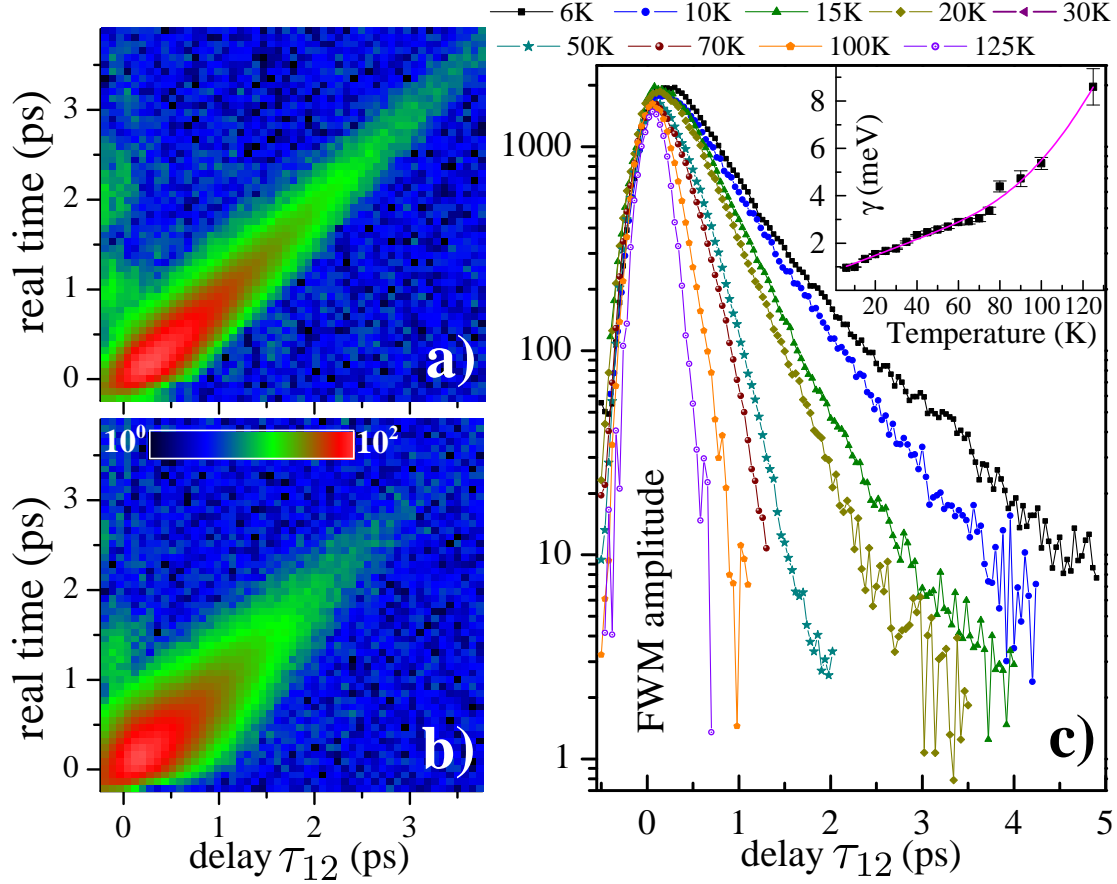


Figure 4: **Impact of a local disorder and temperature on the exciton dephasing in the MoSe<sub>2</sub> monolayer.** a) Time-resolved FWM amplitude, measured on the location displaying a larger  $\xi$ , showing a temporarily narrowed photon echo. The observed increased dephasing time with respect to Fig. 3 attributed to a localization induced increase of the radiative lifetime  $T_1$ . b) as a) but measured on the area showing a broader echo and thus smaller  $\xi$ . A weaker localization yields a shorter  $T_1 = T_2/2$  than in a). Logarithmic color scale over two orders of magnitude. c) FWM amplitude dynamics as a function of temperature measured on the area as in a). Above  $T = 125$  K the dephasing is faster than the temporal resolution of the experiment. The temperature dependent homogenous broadening  $\gamma = 2\hbar/T_2$  (inset) indicates the phonon-induced dephasing mechanism.

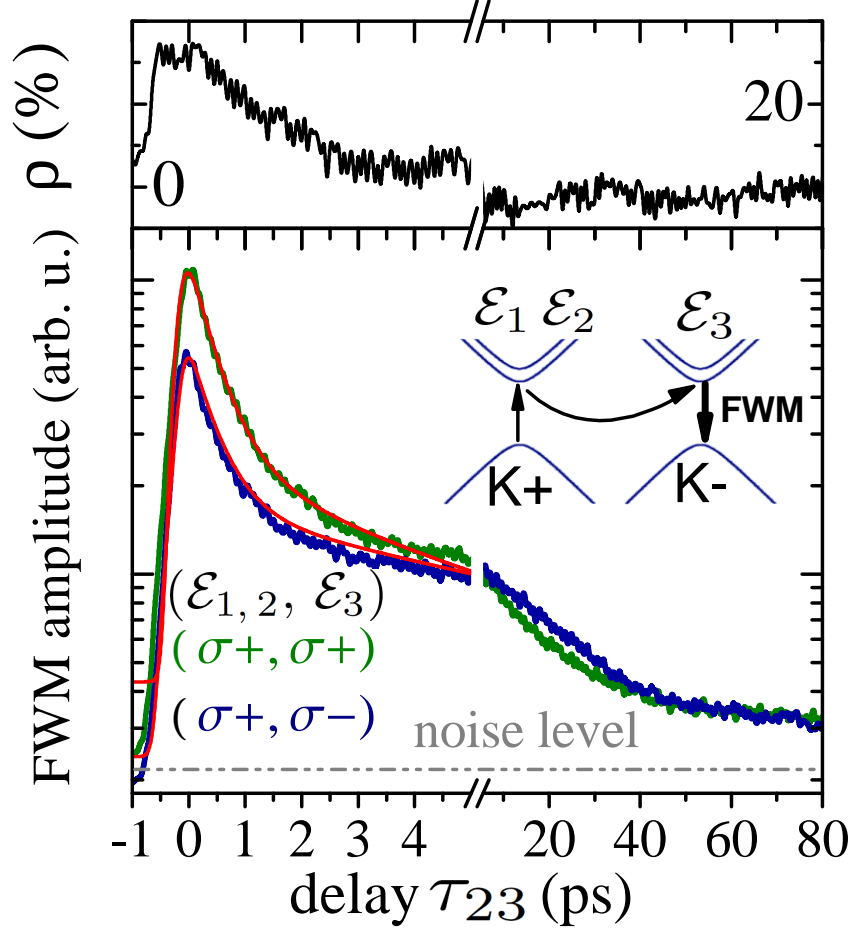


Figure 5: **Inter-valley population dynamics in the MoSe<sub>2</sub> monolayers investigated with the polarization-resolved driving of the FWM.** Bottom: FWM amplitude versus  $\tau_{23}$  of the EX transition obtained at T=6 K upon co- (green circles) and cross-circular (blue squares) setting of  $(\mathcal{E}_{1,2}, \mathcal{E}_3)$ . The modeling, as in Fig. 3 c, is displayed as red lines. Equivalent dynamics have been measured (not shown) for a counter-polarized driving ( $\sigma+ \mapsto \sigma-$ ). Inset: Rationale of the inter-valley dynamics probed with FWM using polarization-resolved driving:  $\mathcal{E}_3$  induces the FWM signal in a given valley, which originates from the population generated in the counter- or co-polarized valley, by setting counter- or co-circular  $\mathcal{E}_{1,2}$ , respectively. Top:  $\tau_{23}$  delay dependence of the measured circular polarization degree,  $\rho(\tau_{23})$ . We measure  $\rho(\tau_{23})$  of several tens of % for initial delays  $\tau_{23}$ , followed by a total depolarization of the FWM, generated by the secondary (see the main text) exciton population.